

# A simulation study of tubercles effect of aerodynamics performance on delta wing

Hamid Yusoff<sup>1,\*</sup>, Dzullijah Ibrahim<sup>1</sup>, Aliff Farhan Mohd Yamin<sup>1</sup>, Mohamad Rafiuddin Abdul Razak<sup>1</sup>, Salina Budin<sup>1</sup>, Shafiq Suhaimi<sup>2</sup>

<sup>1</sup>) Faculty of Mechanical Engineering, Universiti Teknologi MARA, Cawangan Pulau Pinang, Kampung Tok Ebot, 14000, Bukit Mertajam, Pulau Pinang, Malaysia

<sup>2</sup>) Faculty of Mechanical Engineering, Universiti Teknologi MARA, 40450, Shah Alam, Selangor, Malaysia

\*Corresponding e-mail: hamidyusoff@ppinang.uitm.edu.my

**Keywords:** Bio-inspiration; tubercles; delta wing

**ABSTRACT** – The tubercle effect is a recently discovered phenomenon where the sinusoidal pattern ‘bumps’ on the leading edge of an airfoil can improve the aerodynamic performance. This effect was inspired by looking at the humpback whale pectoral flippers that give an exceptional acrobatic maneuverability in the water such as somersaults, also allowing for easier capture of prey. The objective of this research is to study the effect of implementing the tubercles concept on the delta wing in order to see whether it bring advantage or disadvantage in the aerodynamic performance of a delta wing apply on the military aircraft. A delta wing with NACA 64-204, a 5m chord length, 2m tip length and 5m wingspan was designed. A sinusoidal pattern was added to on the edge to resemble the tubercle of a humpback whale. Where model one has 3 bumps, model two has 5 bumps and model three has 7 bumps. The investigation shown that the delta wing with tubercles can increase the lift coefficient by 13.38 %.

## 1. INTRODUCTION

Tubercles referred to the rounded protuberances at the leading edge of airfoils with a sinusoidal pattern shape that can provide improvement in performance under certain condition. It is inspired by humpback whale pectoral flippers that give exceptional acrobatic manoeuvrability such as somersaults; an accomplishment that is novel among Baleen whales [1].

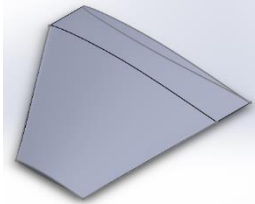
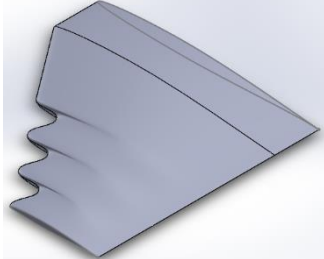
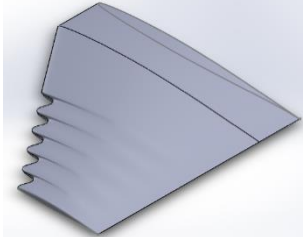
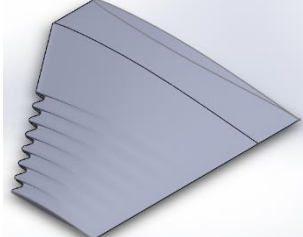
Several of numerical and experimental analysis have been performed to achieve more quality information and better understanding on tubercle concept [2-4]. According to the past studies, the researchers have exposed that the principle impact of leading-edge tubercles on wing performance is softening and delaying of stall [5-6], resulting in the reduction of drag as well increase lift at high angles of attack.

However, the investigation on implementing leading edge tubercles by existing researchers are limited to the airfoil wings rather than delta wing. The objective of this study is to study the effect of tubercles on the aerodynamic performance of a delta wing.

## 2. METHODOLOGY

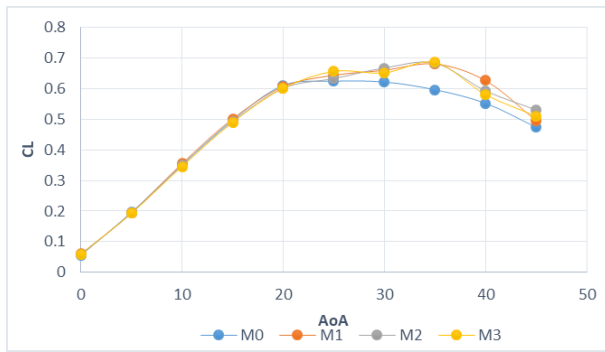
Table 1 shows the four tested delta model with M0 is the Baseline delta wing, M1 is the 3 bumps delta wing, M2 is the 5 bumps delta wing, M3 is the 7 bumps delta wing. Each wing was is tested for lift and drag at 80m/s using computational fluid dynamics (CFD) simulation.

Table 1 Model design.

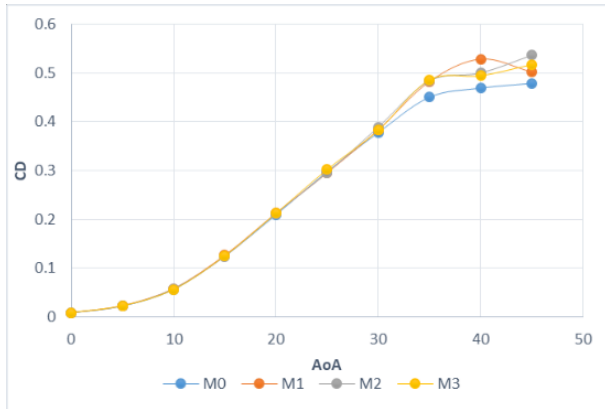
Configuration	Solidworks Models
M0 Baseline	
M1 h = 400 mm λ = 1000 mm	
M2 h = 240 mm λ = 600 mm	
M3 h = 171.43 mm λ = 428.67 mm	

## 3. RESULTS AND DISCUSSION

From Figure 1, for lift coefficient, the value of the M0 indicate better increment compare to M1, M2, M3, before 20° angle of attack. The reduction lift coefficient can be seen after 20° of the angles of attack was shown a M1, M2, M3 was delayed the decreasing of the lift coefficient compare to the M0. This also shown after the stall angle at 20° the M1, M2, and M3 shown a better performance. This answered the hypothesis that tubercles are delaying stall at high angle of attack.



(a)



(b)

Figure 1 Aerodynamics performance where (a) is the lift coefficient vs angle of attack and (b) is the drag coefficient vs angle of attack at  $V=80\text{m/s}$ .

#### 4. CONCLUSION

The configuration of tubercles on delta wing was proved in term of aerodynamics performances such as increasing lift and delayed stall. The configuration of tubercles also improved in flow pattern behind the delta wing which is the flow separation is better compare to

base delta wing because it delayed flow separation. Overall, the implementation of tubercles on the delta wing can delayed stall and the lift coefficient up to 13.38%. However, as the number of tubercles configuration on leading edge of the delta wing increase, the effectiveness toward the aerodynamics performance of the wing decrease.

#### ACKNOWLEDGEMENT

The financial support from Universiti Teknologi MARA, Cawangan Pulau Pinang is highly appreciated.

#### REFERENCES

- [1] Jurasz, C. M., & Jurasz, V. P. (1979). Feeding modes of the humpback whale, *Megaptera novaeangliae*, in Southeast Alaska. *Scientific Reports of the Whales Research Institute*, 31, 69–83.
- [2] Fish, F. E., Weber, P. W., Murray, M. M., & Howle, L. E. (2011). The tubercles on humpback whales' flippers: application of bio-inspired technology. *Integrative and comparative biology*, 51(1), 203-213.
- [3] Stanway, M. J. (2008). *Hydrodynamic effects of leading-edge tubercles on control surfaces and in flapping foil propulsion* (Doctoral dissertation, Massachusetts Institute of Technology).
- [4] Van Nierop, E. A., Alben, S., & Brenner, M. P. (2008). How bumps on whale flippers delay stall: an aerodynamic model. *Physical review letters*, 100(5), 054502.
- [5] Hansen, K. L. (2012). *Effect of leading edge tubercles on airfoil performance* (Doctoral dissertation).
- [6] Miklosovic, D. S., Murray, M. M., Howle, L. E., & Fish, F. E. (2004). Leading-edge tubercles delay stall on humpback whale (*Megaptera novaeangliae*) flippers. *Physics of fluids*, 16(5), L39-L42.

# Experimental test of a standing-wave thermoacoustic rig

Fatimah Al Zahrah Mohd Saat<sup>1,2,\*</sup>, Dahlia Johari<sup>1</sup>, Ernie Mat Tokit<sup>1,2</sup>

<sup>1</sup>) Fakulti Kejuruteraan Mekanikal, Universiti Teknikal Malaysia Melaka, Hang Tuah Jaya, 76100 Durian Tunggal, Melaka, Malaysia

<sup>2</sup>) Centre for Advanced Research on Energy, Universiti Teknikal Malaysia Melaka, Hang Tuah Jaya, 76100 Durian Tunggal, Melaka, Malaysia

\*Corresponding e-mail: fatimah@utem.edu.my

**Keywords:** Standing-wave; thermoacoustics; experiment

**ABSTRACT** – In this paper, an experimental tests of flow inside a standing-wave thermoacoustic rig of two different flow frequencies are reported. The rig consists of a quarter wavelength resonator attached to a loudspeaker that acts as an acoustic driver. A ‘stack’ is located at a location of  $0.18\lambda$  from the pressure antinode. Results showed that the resonance frequency of the two setups are 14.2 Hz and 23.6 Hz, respectively. Measured velocity at several locations indicated that the thermoacoustic flow conditions are achieved. The rig could be used for investigations of fluid dynamics of the less understood oscillatory flow of thermoacoustics.

## 1. INTRODUCTION

Fluid dynamics conditions of an oscillatory flow inside thermoacoustic system is not well known. This leads to difficulties in predicting losses for thermoacoustic based cooler or generator [1]. Earlier investigations reported many special characteristics such as early stage turbulence [2], entrance region [3] and non-linear flow and heat transfer characteristics [4]. These investigations are, however, limited to only several flow conditions. Fluid dynamics changes with operating conditions. Hence more investigations are needed to cover the wide range of thermoacoustic flow conditions. For complex flow conditions, such as those found in thermoacoustics, theoretical solutions are only available for linear model [5]. In most real and complex cases, experimental investigations are needed to help understand the complex nature of the fluid dynamics inside thermoacoustic environment. In order to conduct the fluid dynamic study, an experimental rig that is able of producing the correct oscillatory flow of thermoacoustics environment must be build. In this paper, a test of an experimental rig of a quarter wavelength size with standing wave environment is reported. The rig can be used for detail fundamental investigations of fluid dynamics of an oscillatory flow inside thermoacoustic systems.

## 2. METHODOLOGY

The experimental rig was first designed using DelteEC in order to make sure that thermoacoustic flow conditions could be achieved through the design [6]. Once a correct design is achieved, the experimental rig is build. The experimental rig is as shown in Figure 1. The rig is designed with several segments to allow for investigations of two flow frequencies. The first rig (as is shown in Figure 1) is 6.6 m long while the second rig is

3.8 m long. One side of the resonator is connected to a 700W subwoofer (Model PD180). The input of the loudspeaker is controlled by a DDS function generator and a power amplifier (FLP-MT1201). The loudspeaker is 18 inch in diameter while the resonator is an aluminium duct with a square cross-section of 152.4 mm x 152.4 mm. A loudspeaker box with converging channel is used to connect the subwoofer to the resonator so that standing-wave could be created inside the resonator. A parallel-plate structure (shown as ‘stack’ in Figure 1) is placed at a location of  $0.18\lambda$  from the hard-end of the resonator (the pressure antinode). A piezoresistive sensor (Meggit model 8510B) is used for measuring pressure amplitude of the flow and a hot wire (Sentry model ST732) is used to measure velocity. Sensors are connected to a data logger (Dataq DI-718B) that is fitted with signal conditioner (Model DI-8B41-01). Measured data are processed using Windaq software. The resonator is filled with air at atmospheric pressure.

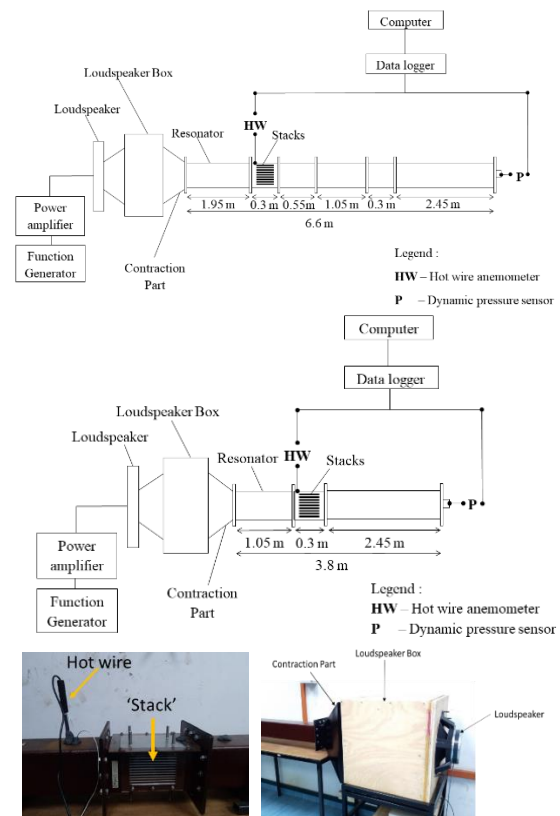


Figure 1 The sechematic diagram of the 6.6 m rig (top), the 3.8 m rig (middle) and pictures of the real rig (bottom).

### 3. RESULTS AND DISCUSSION

For ease of fabrication and instrumentation purposes, the experimental rig was designed according to a quarter wavelength criterion with low frequency range. According to calculation, the 6.6 m long resonator is corresponding to a resonance frequency of 13.1 Hz while the 3.8 m long resonator is corresponding to a resonance frequency of 23.1 Hz. However, experiments are needed to confirm the real value of the resonance frequency for the rig as the presence of additional fixtures, like the loudspeaker box and segmentations of resonator, may lead to changes to the resonance frequency.

#### 3.1 Resonance frequency

The resonance frequency is tested by keeping the voltage input of the loudspeaker at a constant minimum value. The frequency is then varied with an increment of 1 Hz until maximum value of pressure is recorded by the pressure sensor. Figure 2 shows the measured resonance frequency for the 6.6 m long and 3.8 m long resonator, respectively. The drive ratio represents the ratio between the measured value of pressure at antinode and the mean pressure. Results show that the resonance frequency of the 6.6 m long rig is 14.2 Hz and the resonance frequency of the 3.8 m long rig is 23.6 Hz.

#### 3.2 Velocity distribution along resonator

Measurements are done for velocity values in several locations along the resonator. The locations are as defined in Figure 3. Locations A to D represent data from

a 6.6 m long resonator while locations E and F represent data from a 3.8 m long resonator.

The measured values are also compared to the values predicted by the non-linear one-dimensional theory of thermoacoustics. The theoretical results of first order harmonic velocity amplitude,  $u_1$ , are calculated using Equation (1).

$$u_1 = \frac{k \cdot p_a \sin(kx)}{\omega \rho_m} \quad (1)$$

The terms  $k$ ,  $p_a$ ,  $x$ ,  $\omega$  and  $\rho_m$  represent the wave number, pressure amplitude at antinode (hard end), location from the antinode, angular velocity and mean density, respectively. The results are as shown in Figure 4.

In general, both theoretical and experimental values show the same pattern of flow increment as drive ratio increases. Location wise, the velocity amplitude reduces as the flow is approaching the hard end (in the direction from A to D for the 6.6 m long resonator and from E to F for the 3.8 m long resonator). In the experiment, the velocity decreases by 0.41 m/s while the theory predicts a reduction of 1.85 m/s. This corresponds to a difference of around 70% which may be related to 'streaming' or 'non-linear' effects that are not counted in the theoretical equations. Nevertheless, the similar pattern of velocity changes between experiment and theory indicates that a correct thermoacoustic environment have been achieved.

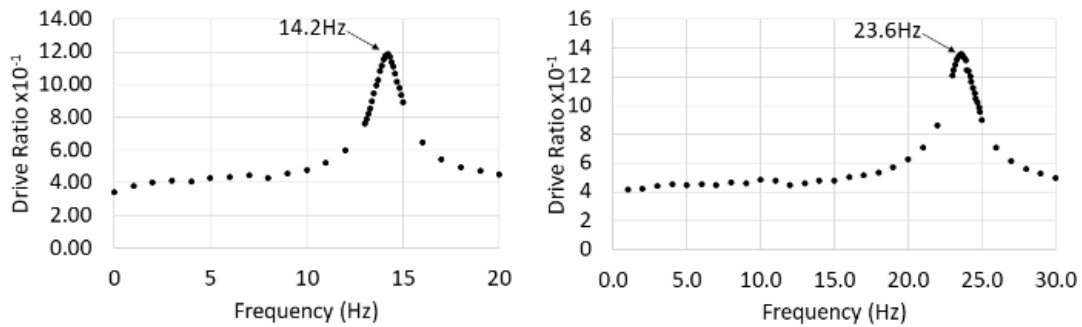


Figure 2 Resonance frequency for the 6.6 m long resonator (left) and the 3.8 m long resonator (right).

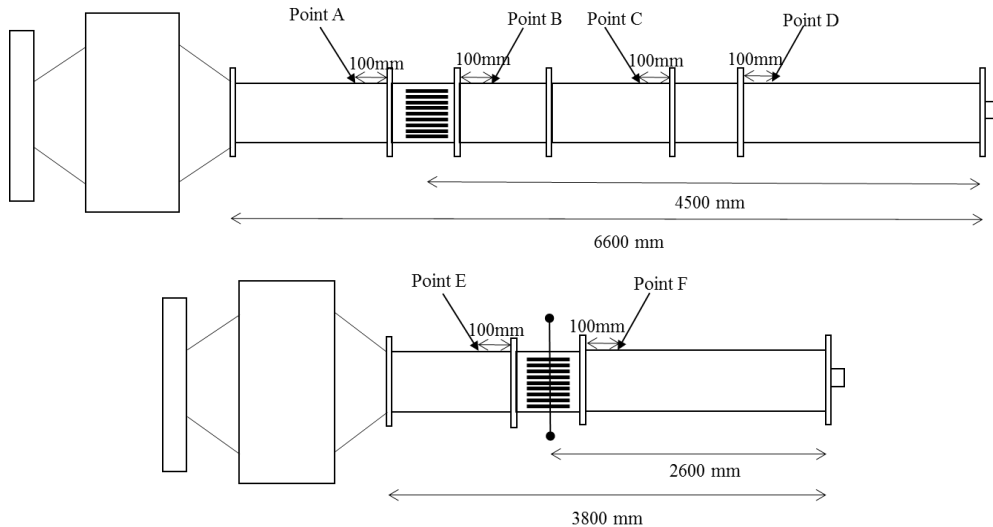


Figure 3 Locations for measurement points along the resonator of 6.6 m long (top) and 3.8 m long (bottom).

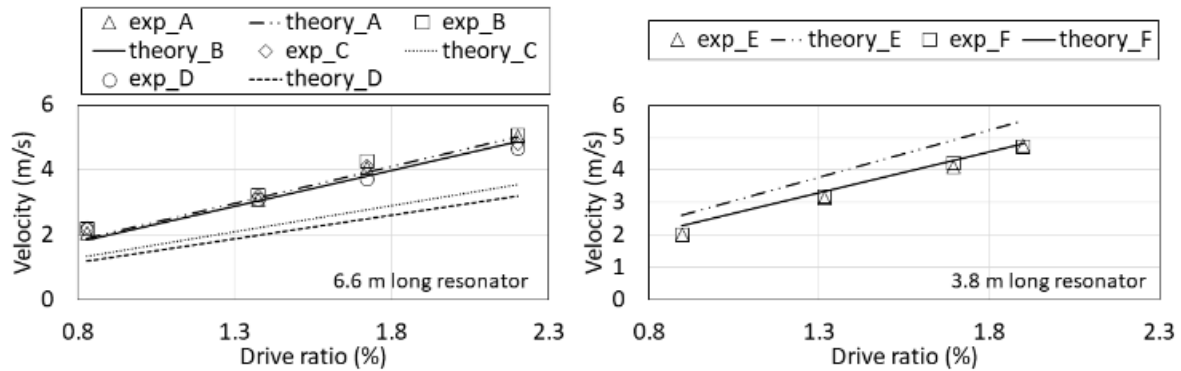


Figure 4 Comparison of velocity amplitude along the resonator between measurement and theoretical values.

#### 4. SUMMARY

Two experimental setups for a standing wave thermoacoustic rig with a quarter wavelength resonator were successfully build with resonance frequency of 14.2 Hz and 23.6 Hz, respectively. The rigs can be used for future investigations of the fluid dynamics phenomena of the less understood thermoacoustic flow conditions.

#### ACKNOWLEDGEMENT

The authors would like to thank Prof. Artur J. Jaworski for his valuable input regarding the experimental measurement practices.

#### REFERENCES

- [1] Abdoulla-Latiwish K. O. A., Mao X., Jaworski A. J. (2017). Thermoacoustic micro-electricity generator for rural dwellings in developing countries by waste heat from cooking activities. *Energy*, 134, 1107-1120.
- [2] Mohd Saat, F.A.Z. and Jaworski, A.J. (2017). Numerical predictions of early stage turbulence in oscillatory flow across parallel plate heat exchangers of a thermoacoustic system. *Applied Sciences*, 7, 673.
- [3] Jaworski, Artur J., Xiaolan Mao, Xuerui Mao, and Zhibin Yu. (2009). Entrance effects in the channels of the parallel plate stack in oscillatory flow conditions. *Experimental Thermal and Fluid Science*, 33(3), 495-502.
- [4] Kuzuu K. and Hasegawa S. (2017). Numerical investigation of heated gas flow in a thermoacoustic device. *Applied Thermal Engineering*, 110, 1283-1293
- [5] Swift G. W., 2002. Thermoacoustics: a unifying perspective for some engines and refrigerators. Sewickley (PA): Acoustical Society of America Publications.

# Simulation study of drying chamber for marine product

Nur Izzati Mohd Azhar<sup>1</sup>, Mohd Afzanizam Mohd Rosli<sup>1,2,\*</sup>, Ahmad Syakir Ghazali<sup>1</sup>, Hiew Sit Jing

<sup>1</sup>Fakulti Kejuruteraan Mekanikal, Universiti Teknikal Malaysia Melaka, Hang Tuah Jaya, 76100 Durian Tunggal, Melaka, Malaysia

<sup>2</sup>Centre for Advanced Research on Energy, Universiti Teknikal Malaysia Melaka, Hang Tuah Jaya, 76100 Durian Tunggal, Melaka, Malaysia

\*Corresponding e-mail: afzanizam@utem.edu.my

**Keywords:** Drying; CFD simulation; velocity; temperature distribution

**ABSTRACT** – Drying chamber is one of the applications in the drying process. This application is widely used in marine product. In this study, a drying chamber for drying process on salted fishes was selected. It able to produce high quality of products in term of drying uniformity and hygienic. The purpose design of drying chamber consists of three trays that are arranged in different levels as a place to dry the products and chimney for the exhaust air. The prediction of the distribution of velocity and temperature in the chamber along the trays has been simulated by CFD which Ansys Fluent 16. The simulation results show that design (b) is most uniform velocity and temperature distribution than design (a).

## 1. INTRODUCTION

Drying is a mass transfer process resulting in the removal of water moisture or moisture from another solvent, by evaporation from a solid, semi-solid or liquid (hereafter product) to end in a solid state [1-3]. The purpose of drying process is to prolong the shelf-life of products and decrease the expenses of transportation and storage capacity. The most famous application in drying is developed drying chamber [4]. The main problem in applied this application is non-uniformity of end product [5-7]. This non-uniformity contributed to the low quality of products. Basically, the parameters that most affected drying air are temperature and velocity [8,9]. Therefore, Computational Fluid Dynamics is used to predict the flow distribution of velocity and temperature in the chamber. CFD simulation is used in order to cut the budget as the experiment needed a lot of budgets, difficult and took a long period of time consuming. CFD simulation also abled to calculated and solved the equations such as conservation of mass, momentum and energy in order to predict the distribution of temperature and velocity. The most significance parameters inside dryers is the uniformity of air distribution because it is determined both the performance and homogeneity of end dried products [7].

In this study, the main objectives of this work are: (i) to predict the distribution of velocity and temperature in the chamber (ii) to analyze best performance between two difference designs.

## 2. METHODOLOGY

### 2.1 CFD Modeling

The drying chamber is designed by consist of three trays that arranged in different level makes a symmetrical

2D flow domain. The model of chamber has been model by Ansys Fluent 16.1. The dimensions of chamber is 1.15m x 0.625m and the thickness of the tray is 0.025 m.

### 2.2 Basic Governing Equations for CFD Simulation

The conservation of mass, momentum and energy for drying air result in the continuity, Navier-Stokes and energy equation respectively [10]. In this study, the simulation was used turbulent model. Following equations are used in this simulation which are:

$$\text{Continuity equation: } \frac{\partial \rho}{\partial t} + \nabla \cdot (\rho \vec{v}) = 0 \quad \dots (1)$$

$$\text{Momentum conservation equations: } \frac{\partial}{\partial t} (\rho \vec{v}) + \nabla \cdot (\rho \vec{v} \vec{v}) = -\nabla p + \nabla \cdot (\vec{\tau}) + \rho \vec{g} + \vec{F} \quad \dots (2)$$

Energy conservation equation:

$$\frac{\partial}{\partial t} (\rho E) + \nabla \cdot (\vec{v} (\rho E + p)) = \nabla \cdot (k_{eff} \nabla T) + S_h \dots (3)$$

### 2.3 Simulation

The simulation was done by using Ansys Fluent 16.1 to solve the governing equations (1), (2) and (3) on to the structured tetrahedral grid. The standard k-e turbulence model was applied in steady state conditions. The boundary conditions were set as follows: (i) inlet: The velocity inlet is 1, 2, 3 m/s, and the air temperature was 0, 20, 30 and 40 °C. (ii) exhaust: The gauge pressure was assumed to be equal to 0 at the outlet.

## 3. RESULTS AND DISCUSSION

### 3.1 Velocity and Temperature Profile

In order to analyze the best performance of drying chamber, there are two data analysis of proposed designs were carried out by using CFD. The most practicable design can be evaluated by comparing the uniformity of air flow distribution in the drying chamber as shown in Figure 1. The distribution of temperature profiles for both designs are shown in Figure 2.

In the design (a), the velocity distribution is poor than design (b). This is because air inlet and exit are small compared to the tray width. For the design (b), it shows sensible in term of uniformity of distribution of temperature in the chamber and tray's zone that close to inlet is preserved maximum temperature. The average velocity and temperature of both designs are calculated. From both designs, it shows that changing the geometrical of drying chamber in term of position of outlet and the size of inlet has some affected on air velocity distribution than temperature distribution.



The increasing angle of divergence can improve the distribution of velocity and relocate exit at the center contributed to the more uniform velocity distribution at the tray zone. Therefore, design (b) can be concluded as the best design compared to the design (a).

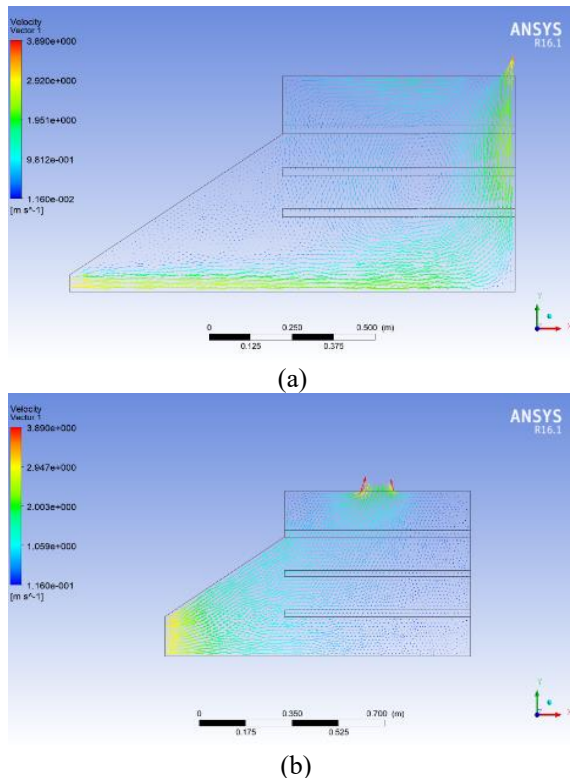


Figure 1 Air velocity distribution profiles for two designs by CFD at inlet air velocity = 3 m/s.

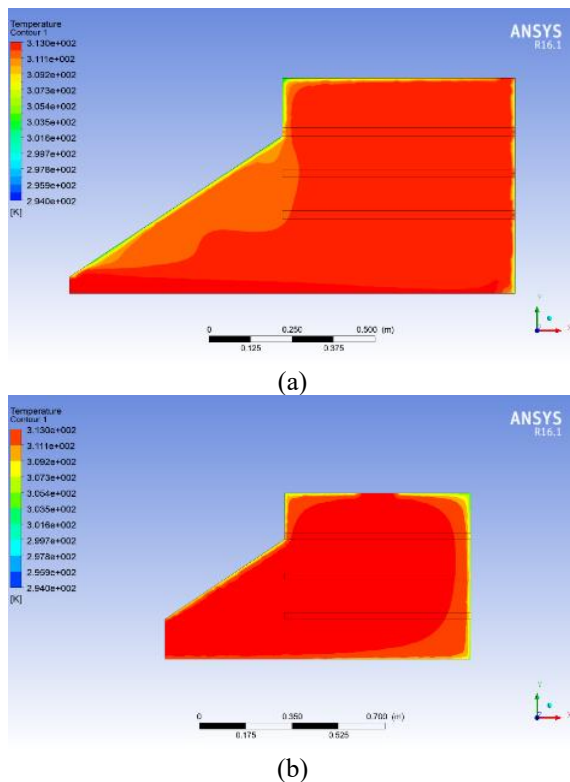


Figure 2 Temperature distribution profiles for two designs by CFD at temperature = 40°C.

#### 4. SUMMARY

Two designs of drying chamber with different position of outlet has been simulated by using ANSYS Fluent 16.1 to investigate the affected of outlet to the uniformity velocity and temperature distribution. From the results of simulation, it showed that the best performance of drying chamber is design (b) as the most uniform of distribution. However, the changing of geometry more affected to the velocity distribution rather than temperature distribution.

#### ACKNOWLEDGEMENT

The authors would like to thank the Fakulti Kejuruteraan Mekanikal and Centre for Advanced Research on Energy of Universiti Teknikal Malaysia Melaka.

#### REFERENCES

- [1] Mujumdar, A. S., & Menon, A. S. (1995). Drying of solids: principles, classification, and selection of dryers. *Handbook of Industrial Drying, 1*, 1-39.
- [2] Noh, A. M., Mat, S., & Ruslan, M. H. (2018). CFD simulation of temperature and air flow distribution inside industrial scale solar dryer. *Journal of Advanced Research in Fluid Mechanics and Thermal Sciences*, 45(1), 156-64.
- [3] Gupta, P. M., Das, A. S., Barai, R. C., Pusadkar, S. C., & Pawar, V. G. (2017). Design and construction of solar dryer for drying agricultural products. *International Research Journal of Engineering and Technology*, 4(3), 1946.
- [4] Amanlou, Y., & Zomorodian, A. (2010). Applying CFD for designing a new fruit cabinet dryer. *Journal of food engineering*, 101(1), 8-15.
- [5] Adams, R. L., & Thompson, J. F. (1985). Improving drying uniformity in concurrent flow tunnel dehydrators. *Transactions of the ASAE*, 28(3), 890-892.
- [6] Mathioulakis, E., Karathanos, V. T., & Belessiotis, V. G. (1998). Simulation of air movement in a dryer by computational fluid dynamics: application for the drying of fruits. *Journal of Food Engineering*, 36(2), 183-200.
- [7] Mirade, P. S. (2003). Prediction of the air velocity field in modern meat dryers using unsteady computational fluid dynamics (CFD) models. *Journal of Food Engineering*, 60(1), 41-48.
- [8] Mulet, A., Bernal, A., Borr, M., & Pinaga, F. (1987). Effect of air flow rate on carrot drying. *Drying technology*, 5(2), 245-258.
- [9] Karathanos, V. T., & Belessiotis, V. G. (1997). Sun and artificial air drying kinetics of some agricultural products. *Journal of Food Engineering*, 31(1), 35-46.
- [10] Yongson, O., Badruddin, I. A., Zainal, Z. A., & Narayana, P. A. (2007). Airflow analysis in an air conditioning room. *Building and Environment*, 42(3), 1531-1537.

# Investigation of heat effects on electronic sensors in a lightning detection system

Tuan Nurul Husna Tuan Zakaria<sup>1,\*</sup>, Maslan Zainon<sup>2</sup>, Maaspaliza Azri<sup>1</sup>, Zikri Abadi Baharudin<sup>2</sup>, Ahmad Aizan Zulkefle<sup>2</sup>, Ahmad Idil Abdul Rahman<sup>2</sup>, Mohd Ariff Mat Hanafiah<sup>2</sup>, Shahrudin Zakaria<sup>2</sup>

<sup>1</sup>) Fakulti Kejuruteraan Elektrik, Universiti Teknikal Malaysia Melaka, Hang Tuah Jaya, 76100 Durian Tunggal, Melaka, Malaysia

<sup>2</sup>) Fakulti Teknologi Kejuruteraan Elektrik dan Elektronik, Universiti Teknikal Malaysia Melaka, Hang Tuah Jaya, 76100 Durian Tunggal, Melaka, Malaysia

\*Corresponding e-mail: husnazakaria94@gmail.com

**Keywords:** Heat effects; electronic sensors; lightning detection system

**ABSTRACT** – This paper describes the investigation of a lightning detection system that focuses on heat effects on electronic sensors. The study involves designing and performing simulations of a lightning detection circuit with several types of Integrated Circuits (ICs). BUF602, LMH6559, and THS4631 ICs were used to determine how heat from solar radiation can affect their performances. OrCAD software was used to simulate and analyse a series of data via electric field measurements.

## 1. INTRODUCTION

Integrated circuits are circuits composed of transistors, diodes, resistors, and capacitors fabricated on a single chip of semiconductor material. Each of these integrated circuits is designed and built to withstand particular amounts or level of heat. When overheating occurs, the ability and performance of integrated circuits are affected. Thus, this research paper explores and discusses the effects of heat on electronic components in a lightning detection system.

The primary goal of this research is to design and simulate a lightning detection circuit with several types of integrated circuits (ICs) or sensors, which are BUF602, LMH6559 and THS4631, mainly due to their economic values and accessibility. The schematic diagrams of these three different types of ICs were designed in OrCAD software.

Overheating can potentially affect or even damage electric components, which the causes of overheating and how to protect electronic components from the damaging effects of excessive heat were explained with some recommendations by Almubarak [1].

Integrated circuits are semiconductor devices that mostly made of Silicon materials, however, many researchers had also been conducted to study the performance of integration between Silicon and Germanium semiconductors [2][3][4]. ICs in electronic

devices that operated at elevated temperature is a major cause of failures and a critical problem in developing more advanced electronic packages. Thermal management issues such as heat dissipation from the electronic control unit need to be resolved [5].

Temperature is the main factor or source attributed to the efficient performance of electronic components since there is a relationship between the performances, including the lifecycle of electronic components and its particular range of operating temperature [6,7].

Among other factors, lightning is a major contributor to electrical power disruptions. For many years Eskom has had to improvise to make sure the most effective mitigation methods and applications to address the impact of lightning on the delivery of power within its operational border [8].

## 2. METHODOLOGY

The circuit development for electronic sensors in a lightning detection system is divided into two sections, which are the software and hardware. The design of the modelling circuits must be determined and simulated accordingly prior to designing and constructing the related hardware. This paper focuses on the software section.

Initially, for example in THS4631 circuit, the circuit modelling was designed in OrCAD software and the compatibility of the circuit output must be determined whether it was feasible to be used in this research or vice versa. After the circuit was successfully simulated in OrCAD software, the next stage was to design the PCB layout, and then proceeded to its hardware development. This part consists of all the selected ICs; BUF602, LMH6559, and THS4631. Figure 1 shows the schematic diagram of one of the ICs that was designed and successfully simulated.

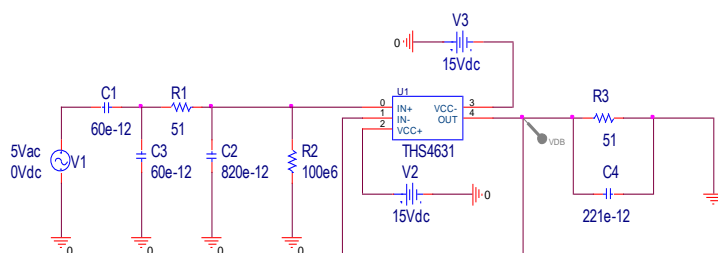


Figure 1 Schematic diagram for THS4631.



Figure 2 depicts the system measuring scheme by which at the sensor stage, the plate of antenna was set at a specific location and connected to the input using a Bayonet Neill-Concelman (BNC) cable. The output was connected to the compensator and Yokogawa oscilloscope to record the data waveform that occurred when a lightning strike is detected. The combination of the circuit and antenna was set up as one detection system at the investigation station.

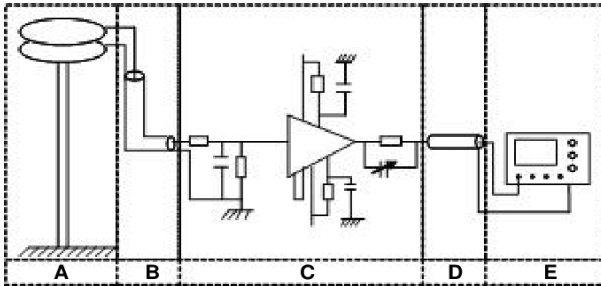


Figure 2 Scheme of the measuring system. (A) antenna, (B) short coaxial cable, (C) electronic circuit, (D) long coaxial cable, (E) recording equipment.

In this research, the data of heat effects on BUF602, LMH6559, and THS4631 were determined from the measured waveforms by using an OrCAD software. These data were compared to investigate and analyse to determine which of the integrated circuits is the most suitable to be used in a lightning detection system.

### 3. RESULTS AND DISCUSSION

Figure 3 represents the preliminary result of a waveform from the simulated circuit for THS4631.

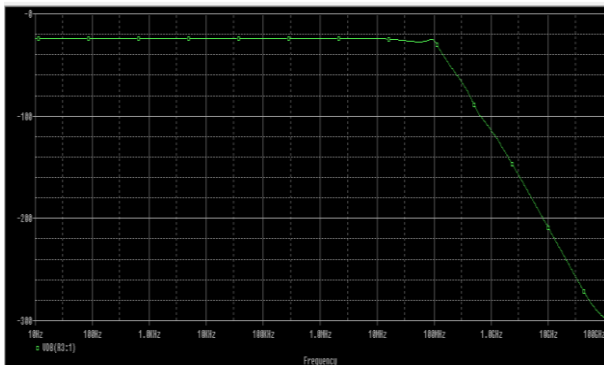


Figure 3 Waveform result of THS4631.

The emergence of this waveform simulation result can be attributed to a certain level of heat effect for the electronic sensor. In order to investigate the actual heat effects on electronic sensors in a lightning detection system, all of the electric field waveform results will be compared according to the changes of temperatures that occur inside the electronic control box. The results can further determine the sensors' performances, particularly for their time rising and zero crossing parameters.

### 4. CONCLUSION

Lightning is a universe's natural phenomenal activity that always manage to attract interests of many researchers in their studies. Lightning is a universe natural phenomenon activity that always attracts the

interest of many researchers in their studies. In Malaysia, the effects of heat on electronic sensors in a lightning detection system are yet to be further investigated in obtaining reliable data. This research is one of the initial steps towards the stated investigation, which involved designing and performing simulations of a lightning detection circuit with several types of integrated circuits by using an OrCAD software. BUF602, LMH6559, and THS4631 ICs were selected and used as the electronic sensors, which the data results were compared to determine which of the integrated circuits has the best performance and suitable to be implemented in a lightning detection system.

### REFERENCES

- [1] Almubarak, A. A. (2017). The effects of heat on electronic components. *Int. J. Eng. Res. Appl.*, 7(5), 52–57.
- [2] Zulkefle, A. A., Zainon, M., Zakaria, Z., Hanafiah, M., Ariff, M., Razak, N. H. A., ... & Amin, N. (2015). A comparative study between silicon germanium and germanium solar cells by numerical simulation. *Applied Mechanics and Materials*, 761, 341-346.
- [3] Mohamad, R. T., Zulkefle, A. A., Baharudin, Z. A., Rahman, A. A., Zainon, M., Hanafiah, M. A. M., Salim, S. N. S., Abu Shah, I., Ibrahim, M., Adnan, H., Amran, A. C., Ibrahim, I. M., Abdullah, L., Aman, O., Raja Abd Rahman, R. R., & Adnan, W. A. W. (2015). Effect of temperature on 1 micron thick silicon solar cell. *International Journal of Applied Engineering Research*, 10(11), 29127-29133.
- [4] Zulkefle, A. A., Zainon, M., Zakaria, Z., Shahahmadi, S. A., Bhuiyan, M. A. M., Alam, M. M., Sopian, K., & Amin, N. (2013). Effects of germanium layer on silicon/germanium superlattice solar cells. In *2013 IEEE 39th Photovoltaic Specialists Conference (PVSC)* (pp. 3484-3486).
- [5] Ekpu, M., Bhatti, R., Ekere, N., Mallik, S., Amalu, E., & Otiaba, K. (2011). Investigation of effects of heat sinks on thermal performance of microelectronic package. In *3rd IEEE International Conference on Adaptive Science and Technology (ICAST 2011)* (pp. 127-132).
- [6] Lakshminarayanan, V., & Sriraam, N. (2014, January). The effect of temperature on the reliability of electronic components. In *2014 IEEE International Conference on Electronics, Computing and Communication Technologies (CONECCT)* (pp. 1-6).
- [7] [Watson, J., & Castro, G. (2012). High-temperature electronics pose design and reliability challenges. *Analog Dialogue*, 46(2), 3-9.
- [8] Evert, R., & Schulze, G. (2005). Impact of a new lightning detection and location system in South Africa. In *2005 IEEE Power Engineering Society Inaugural Conference and Exposition in Africa* (pp. 356-363).

# Mathematical modeling of two-phase flow under Dusty Williamson fluid model

N.S. Arifin, S.M. Zokri, A.R.M. Kasim\*, M.Z. Salleh

Applied & Industrial Mathematics Research Group, Faculty of Industrial Sciences & Technology,  
Universiti Malaysia Pahang, 26300 UMP Kuantan, Pahang, Malaysia

\*Corresponding e-mail: rahmanmohd@ump.edu.my

**Keywords:** Aligned magnetic field; two-phase flow; dusty Williamson fluid

**ABSTRACT** – A physical phenomenon involving two-phase system (fluid and solid) is encountered in many applications like air or water pollution, blood flow in arteries, flows in rocket tubes, sedimentation and fluidized bed. In all of these implementations, the suitable knowledge concerning such system is very essential for predicting the behavior of the flow processes to obtain the expected outcome. Therefore, this paper provides some theoretical assumptions of the possible scenarios occurring in the particular flow system by presenting the mathematical model of two-phase flow. Specifically, the Williamson fluid flow in the presence of dust particles is analyzed with the amalgamate influences of buoyancy force, modified magnetic field and thermal condition of Newtonian heating. The rheology of the respective two-phase flow model is characterized by a set of partial differential equations, which describes its physical properties.

## 1. INTRODUCTION

In many practical circumstances such as impurities in common fluid, combustion chambers, environmental pollutants, fluidized beds, treatment of waste-water and petroleum industry draw heavily on two-phase flow system [1]. Moreover, the contamination of solid particles (ash and shoot) exerts a profound influence on the performance of combustion MHD generators and plasma MHD accelerators which then instigates a number of studies relating to two-phase flow system associated with uniform magnetic field [2-3]. Besides, the recent mathematically studied has been done by [4-5]. In connection to these studies, the present investigation aims to give a special focus on the application of modified magnetic field to non-Newtonian Williamson fluid flow embedded with dust particles from the perspectives of mathematical analysis.

Among non-Newtonian fluids, Williamson fluid with the capability to portray the characteristics of both elastic and viscous effects has also engaged attention of many researchers. Furthermore, the flow of Williamson fluid containing solid particles is an important preamble to the understanding of behaviour of blood in stenosed arteries, polymer solution and chyme in small intestine by assuming the whole system as fluid-solid suspension. This paper endeavours to account for the two-phase flow properties of Williamson fluid over a vertical stretching sheet.

## 2. METHODOLOGY

### 2.1 Mathematical Formulation

A steady two-dimensional incompressible dusty Williamson fluid over a vertical stretching sheet has been considered. The sheet is stretched with uniform velocity,  $u_w(x) = ax$  and magnetic field is inclined at angle  $\alpha_1$  to the flow direction, as shown in Figure 1. Note that, the following assumptions for dust particles are adapted, in which the dust particles are in spherical shape, uniform size and number density of these are taken as constant throughout the flow.

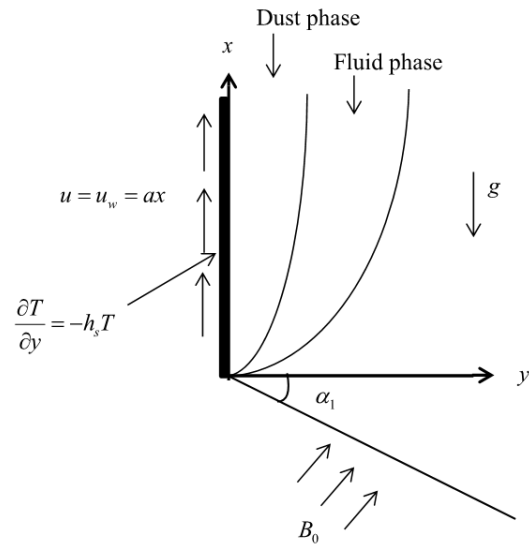


Figure 1 Flow configuration.

The governing boundary layer equations for this two-phase model can be written as

Fluid phase:

$$\frac{\partial u}{\partial x} + \frac{\partial v}{\partial y} = 0, \quad (1)$$

$$u \frac{\partial u}{\partial x} + v \frac{\partial u}{\partial y} = \frac{\mu_0}{\rho} \left( \frac{\partial^2 u}{\partial y^2} + \sqrt{2} \Gamma \frac{\partial u}{\partial y} \frac{\partial^2 u}{\partial y^2} \right) + \frac{\rho_p}{\rho \tau_v} (u_p - u) - \frac{\sigma}{\rho} B_0^2 \sin^2 \alpha_1 u + \beta^* g (T - T_\infty), \quad (2)$$

$$\rho_\infty c_p \left( u \frac{\partial T}{\partial x} + v \frac{\partial T}{\partial y} \right) = k \left( \frac{\partial^2 T}{\partial y^2} \right) + \frac{\rho_p c_s}{\gamma_T} (T_p - T), \quad (3)$$

Dust phase:

$$\frac{\partial u_p}{\partial x} + \frac{\partial u_p}{\partial y} = 0, \quad (4)$$

$$\rho_p \left( u_p \frac{\partial u_p}{\partial x} + v_p \frac{\partial u_p}{\partial y} \right) = \frac{\rho_p}{\tau} (u - u_p), \quad (5)$$

$$\rho_p c_s \left( u_p \frac{\partial T_p}{\partial x} + v_p \frac{\partial T_p}{\partial y} \right) = -\frac{\rho_p c_s}{\gamma_T} (T_p - T). \quad (6)$$

The boundary conditions associated with the model are

$$u = u_w(x), v = 0, -k(\partial T / \partial y) = h_f(T_f - T) \text{ at } y = 0 \quad (7)$$

$$u \rightarrow 0, u_p \rightarrow 0, v_p \rightarrow v, T \rightarrow T_\infty, T_p \rightarrow T_\infty \text{ at } y \rightarrow \infty$$

The similarity transformations for both phases are

$$u = axf'(\eta), v = -\sqrt{av}f(\eta), \eta = \sqrt{\frac{a}{v}}y, u_p = axF'(\eta), \quad (8)$$

$$v_p = -\sqrt{av}F(\eta), \theta(\eta) = \frac{T - T_\infty}{T_\infty}, \theta_p(\eta) = \frac{T_p - T_\infty}{T_\infty},$$

By using Equation (8), Equations (1)-(7) become

$$f'''(\eta) + f(\eta)f''(\eta) - (f'(\eta))^2 + \lambda_1 f''(\eta)f'''(\eta) + \beta N(F'(\eta) - f'(\eta)) - M \sin^2 \alpha_1 f'(\eta) + \lambda \theta(\eta) = 0, \quad (9)$$

$$\theta''(\eta) + \text{Pr} f(\eta)\theta'(\eta) + \frac{2}{3}\beta N(\theta_p(\eta) - \theta(\eta)) = 0, \quad (10)$$

$$(F'(\eta))^2 - F(\eta)F''(\eta) + \beta(F'(\eta) - f'(\eta)) = 0, \quad (11)$$

$$\theta_p'(\eta)F(\eta) + \frac{2}{3}\frac{\beta}{\lambda \text{Pr}}(\theta_p(\eta) - \theta(\eta)) = 0, \quad (12)$$

and the transformed boundary conditions become

$$f(0) = 0, f'(0) = 1, \theta'(0) = -b(1 - \theta(0)) \text{ at } \eta = 0 \quad (13)$$

$$f'(\eta) \rightarrow 0, F'(\eta) \rightarrow 0, \theta(\eta) \rightarrow 0, \theta_p(\eta) \rightarrow 0 \text{ as } \eta \rightarrow \infty$$

Note that,  $\beta, N, M, \alpha_1, \lambda, \text{Pr}, \gamma$  and  $b$  are the physical parameters of fluid-particle interaction, mass concentration of particle phase, magnetic field, aligned angle, mixed convection, Prandtl number, specific heat ratio of mixture and Biot number.

## 2.2 Numerical Computation

Equations (9)-(13) have been solved by using the Keller-box method in Matlab software. The finite boundary layer thickness of  $\eta_\infty = 8$  is selected for boundary conditions to fully satisfied.

## 3. RESULTS AND DISCUSSION

To ascertain the present results, the validation has been made by a direct comparison with existing outcome in literature. The comparative values displayed in Table 1 are in a good agreement, which shows reliability in the numerical solutions obtained.

Figures 2 and 3 illustrated the influences of fluid particle interaction parameter  $\beta$  on velocity and temperature profiles. The velocity and temperature profiles of fluid phase are reported to decrease with the increase value of  $\beta$ . In contrast, the opposite behavior occurs for dust phase when  $\beta$  increased. Physically, the growing effect of  $\beta$  reduces the relaxation time of dust particles which then motivates the dust particles motion so that the equilibrium stage between their velocities and fluid velocity is achieved. Additionally, the fluid temperature decreases as the thermal relaxation time is also reduced.

Table 1 Comparative values of  $-f''(0)$  when  $\text{Pr} = 10$ ,

$$N = \beta = \lambda = 0, \alpha_1 = \pi/2, \gamma \rightarrow \infty.$$

$M$	Fathizadeh et al. [6]	Present
0	1.00000	1.00000
1	1.41421	1.41421
5	2.44948	2.44949
10	3.31662	3.31662

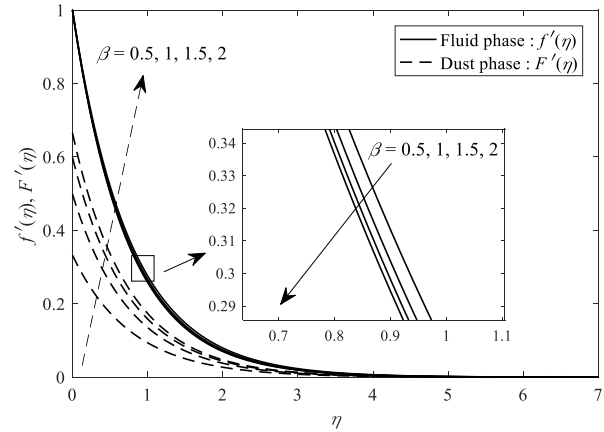


Figure 2 Velocity profile for various values of  $\beta$ .

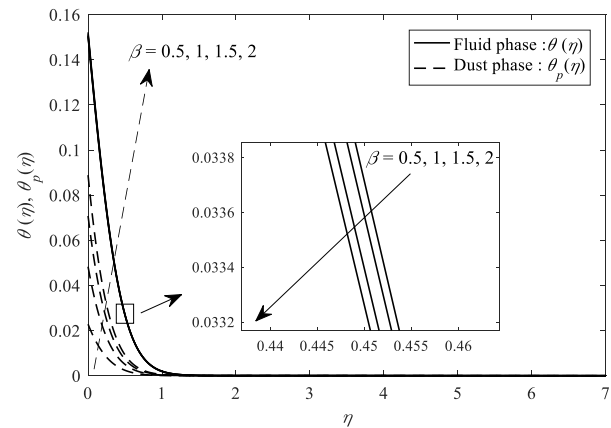


Figure 3 Temperature profile for various values of  $\beta$ .

## 4. CONCLUSION

Exploration into the analysis of fluid-solid system has shown that the accumulation of dust particles near the wall could reduce the performance of certain engineering devices. Thus, it is envisaged that the present solutions will contribute to the understanding of behavior in this system by providing anticipating outcomes. Note that,  $\beta$  has influenced the flow and temperature of fluid as well as dust phases, respectively.

## ACKNOWLEDGMENT

The authors gratefully acknowledge the financial support received Universiti Malaysia Pahang (UMP) under RDU 170328 and RDU 190303.

## REFERENCES

- [1] Siddiqua, S., Begum, N., Hossain, M. A., & Gorla, R. S. R. (2017). Natural convection flow of a two-phase dusty non-Newtonian fluid along a vertical surface. *International Journal of Heat and Mass Transfer*, 113, 482-489.

- [2] Venkateshappa, V., Rudraswamy, B., Gireesha, B. J., & Gopinath, K. (2008). Viscous dusty fluid flow with constant velocity magnitude. *Electronic Journal of Theoretical Physics*, 5(17), 237-252.
- [3] Nandkeolyar, R., & Sibanda, P. (2013). On convective dusty flow past a vertical stretching sheet with internal heat absorption. *Journal of Applied Mathematics*, 2013.
- [4] Arifin, N. S., Zokri, S. M., Kasim, A. R. M., Salleh, M. Z., & Mohammad, N. F. (2018). Aligned magnetic field flow of Williamson fluid over a stretching sheet with convective boundary condition. *MATEC Web of Conferences*, 189, 11005.
- [5] Arifin, N. S., Zokri, S. M., Kasim, A. R. M., Salleh, M. Z., & Mohammad, N. F. (2019). Two-Phase Mixed Convection Flow of Dusty Williamson Fluid with Aligned Magnetic Field over a Vertical Stretching Sheet. In *Proceedings of the Third International Conference on Computing, Mathematics and Statistics (iCMS2017)* (pp. 209-216). Springer, Singapore.
- [6] Fathizadeh, M., Madani, M., Khan, Y., Faraz, N., Yildirim, A., & Tutkun, S. (2013). An effective modification of the homotopy perturbation method for mhd viscous flow over a stretching sheet. *Journal of King Saud University-Science*, 25(2), 107-113.

# Turbulence measurements in the centerline region of a turbulent round jet using a software-driven laser doppler system

Mohd Rusdy Yaacob<sup>1,\*</sup>, Preben Buchhave<sup>2</sup>, Clara Marika Velte<sup>3</sup>

<sup>1)</sup> Fakulti Kejuruteraan Elektrik, Universiti Teknikal Malaysia Melaka, Hang Tuah Jaya, 76100 Durian Tunggal, Melaka, Malaysia

<sup>2)</sup> Intarsia Optics, Sønderkovvej 3, 3460 Birkerød, Denmark

<sup>3)</sup> Department of Mechanical Engineering, Technical University of Denmark, 2800 Kgs. Lyngby, Denmark

\*Corresponding e-mail: rusdy@utem.edu.my

**Keywords:** Turbulent round jet; laser Doppler anemometer; turbulence measurements

**ABSTRACT** – This paper demonstrates turbulence measurements of a turbulent round jet. It is aimed to map the energy cascade and turbulent scales along the jet centerline, spanning from the developing region to the fully developed counterpart. Measurements were performed using a software-driven LDA system, which was tested and proven to deliver high accuracy measurements. The velocity static moments show a similar trend with previous jet studies, as expected. The spatial kinetic energy spectra and second-order structure functions have been compared to the Kolmogorov -5/3 and 2/3 power laws. Good agreement is only obtained in the fully developed region.

## 1. INTRODUCTION

An axisymmetric turbulent round jet has been considered as a classical flow problem since this in principle simple flow still exhibits many of the elementary physical behavior patterns of turbulent flow [1]. Experimental investigation on it will therefore be significant in solving different kinds of problems identified in various types of flow processes [2]. Measurement wise, the centerline region is considered less challenging compared to the shear region, where the velocity fluctuation and turbulence intensity are much higher [3]. Investigation on this region may therefore be not as central as across the shear layer but a higher resolution and rigorous measurement along the jet centerline can be of the great interest in mapping the energy cascade and turbulent scales in the centerline region. This even becomes more essential when the measurements are performed using a novel and sophisticated laser Doppler system [4], which has been proven to function robustly even in the more difficult regions of the jet [5]. In fact, a significantly higher data rate is also expected from the measurements in the centerline region, which allows us to compute more accurately and obtain meaningful plots of the higher order turbulence statistics.

## 2. METHODOLOGY

Measurements were performed along the jet centerline (exit diameter,  $D=10$  mm) to investigate the centerline profiles of the mean streamwise velocity and its higher order statistics. The measurement points range from  $x/D=10$  up to  $x/D=37$ , with 10 mm increments between each point (see Figure 1), which should cover both the non-equilibrium (developing) and equilibrium

(fully developed) regions of the jet. The exit velocity was set to nearly 40 m/s that corresponds to a jet exit Reynolds number,  $Re \approx 25000$ . The data was then transferred to a computer for signal processing and data interpretation using our in-house LDA processing software, which has been thoroughly described in [4,5].

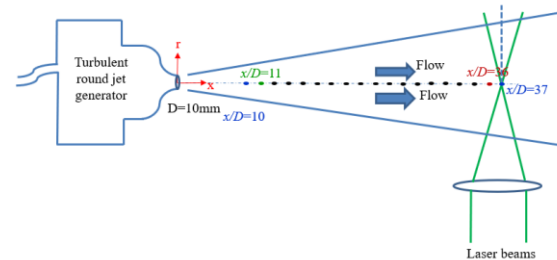


Figure 1 Distribution of measurement points along the jet centerline.

## 3. RESULTS AND DISCUSSION

The mean streamwise velocity, velocity variance and turbulence intensity profiles with downstream distance along the centerline are displayed in Figure 2. The first two of these decay approximately inversely proportionally with the downstream distance, as expected, with a faster decay in the developing region [6][7]. The turbulence intensity builds up more gradually in the developing region and asymptotes to a nominal value of around 24% in fully developed counterpart.

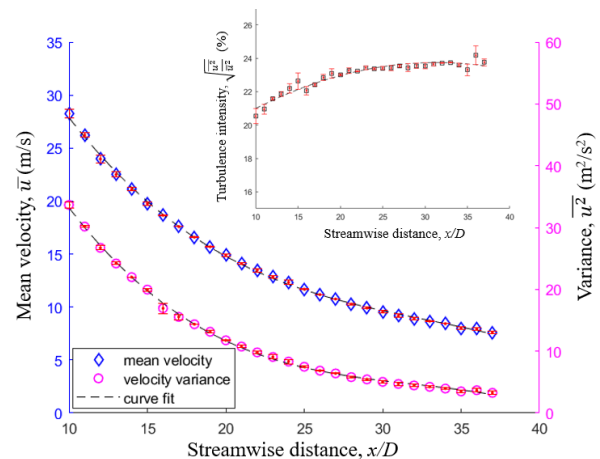


Figure 2 The downstream profiles of mean streamwise velocity, velocity variance and turbulence intensity, with 3<sup>rd</sup>-order polynomial fit.

Further, the energy spectra were also computed, which describe the distribution of turbulent kinetic energy,  $E$  across different wavenumbers,  $k$  of the flow (see Figure 3). Each spectrum is deliberately normalized in the low wave number asymptote for a better comparison in shapes. The shape of the spectrum corresponding the fully developed region ( $x/D \geq 25$ ) appears to nearly follow the  $-5/3$  slope as postulated by the Kolmogorov  $-5/3$  law [8][9]. The spectra obtained in the non-equilibrium counterpart revealed a symptom of invalidity of the law.

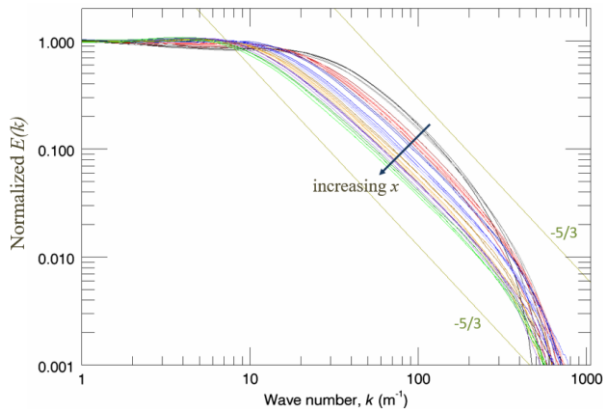


Figure 3 Downstream development of spatial turbulent kinetic energy spectra. Following arrow direction:  $x/D=10, 11, 12, 13, 14, 15, 16, 17, 18, 19, 20, 21, 22, 23, 24, 25, 26, 27, 28, 29, 30, 31, 32, 33, 34, 35, 36, 37$ .

The second order structure functions,  $S_2(\ell)$  are plotted in Figure 4 to show the development of turbulent scales,  $\ell$  across the jet centerline. The large scales are seen to grow, and more large-scale activity is relatively noticed in the downstream direction. The tendency to follow the  $2/3$  slope is again higher in the equilibrium region compared to the non-equilibrium counterpart [10,11].

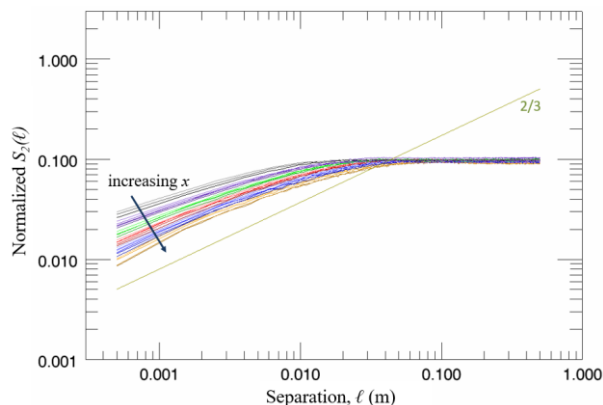


Figure 4 Downstream development of spatial second order structure functions. Following arrow direction:  $x/D=10, 11, 12, 13, 14, 15, 16, 17, 18, 19, 20, 21, 22, 23, 24, 25, 26, 27, 28, 29, 30, 31, 32, 33, 34, 35, 36, 37$ .

#### 4. CONCLUSION

Measurements have been successfully performed to map the energy cascade and turbulent scales along the jet centerline, while revealing different degree of validity of the Kolmogorov  $-5/3$  and  $2/3$  laws. The disagreement to

the laws found in the developing region open doors to work on deeper statistical analysis, which can be useful for numerical turbulence modelers.

#### ACKNOWLEDGEMENT

The authors wish to acknowledge the support of Ministry of Education Malaysia, DTU Mechanical Engineering, Reinholdt W. Jorek og Hustrus Fond (grant journal no. 13-J9-0026), Fabriksejer, Civilingeniør Louis Dreyer Myhrwold og hustru Janne Myhrwolds Fond (grant journal no. 13-M7-0039, 15-M7-0031 and 17-M7-0035) and Siemens A/S Fond grant no. 41.

#### REFERENCES

- [1] Capp, S. P. (1984). Experimental investigation of the turbulent axisymmetric jet. State University of New York, Buffalo.
- [2] Islam, M. T., & Ali, M. A. T. Flow characteristics of a turbulent axisymmetric jet. *J. Inst. Eng. (India). Mech. Eng. Div.*, 76, 65–71.
- [3] Yaacob, M. R., Schlender, R. K., Buchhave, P., & Velte, C. M. (2018). Mapping of the turbulent round jet developing region using a constant temperature anemometer (CTA). *Malaysian Journal of Fundamental and Applied Sciences*, (Special Issue on Natural Sciences and Mathematics (ESCon 2018)), 443-446.
- [4] Yaacob, M. R., Schlender, R. K., Buchhave, P., & Velte, C. M. (2018). Validation of improved laser Doppler anemometer (LDA) based on the fully developed turbulent round jet. In *Symposium on Electrical, Mechatronics and Applied Science 2018*.
- [5] Yaacob, M. R., Schlender, R., Buchhave, P., & Velte, C. M. (2018). Experimental evaluation of Kolmogorov's  $-5/3$  and  $2/3$  power laws in the developing turbulent round jet," *Journal of Advanced Research in Fluid Mechanics and Thermal Sciences*, 45(2), 14–21.
- [6] Grandchamp, X., Van Hirtum, A., & Pelorson, X. (2013). Centreline velocity decay characterisation in low-velocity jets downstream from an extended conical diffuser. *Meccanica*, 48(3), 567-583.
- [7] Ball, C. G., Fellouah, H., & Pollard, A. (2012). The flow field in turbulent round free jets. *Progress in Aerospace Sciences*, 50, 1-26.
- [8] Batchelor, G. K. (1953). *The theory of homogeneous turbulence*. Cambridge university press.
- [9] George, W. K., & Gibson, M. M. (1992). The self-preservation of homogeneous shear flow turbulence. *Experiments in fluids*, 13(4), 229-238.
- [10] Danaila, L., Anselmetti, F., & Antonia, R. A. (2002). An overview of the effect of large-scale inhomogeneities on small-scale turbulence. *Physics of Fluids*, 14(7), 2475-2484.
- [11] Romano, G. P., & Antonia, R. A. (2001). Longitudinal and transverse structure functions in a turbulent round jet: effect of initial conditions and Reynolds number. *Journal of Fluid Mechanics*, 436, 231-248.



# The application of spectral methods in two-dimension fluid flow

Farida Nurmala Sihotang\*, Diyah Wijayati, Robi Dany Riupassa

Program Studi Teknik Informatika, Sekolah Tinggi Teknologi Bandung,  
Bandung, 40235 Bandung, Jawa Barat, Indonesia

\*Corresponding e-mail: farida@sttbandung.ac.id

**Keywords:** Vorticity; spectral methods; fluid

**ABSTRACT** – Spectral method is a numerical method for solving partial differential equation using Fourier transform. The application of Fourier transform is changes differential equation into ordinary equation. The differential equation is used in 2D fluid flow turbulence problem governed by incompressible constant density Navier Stokes equation.

## 1. INTRODUCTION

In this paper we will consider the 2D turbulence problem where flow is governed by incompressible constant density Navier Stokes equation. Navier Stokes equation is differential equation for 2D case who's interesting to discuss. The solution of the equation needs numerical approach. The numerical methods will use spectral method with Fourier series expansion. The spectral methods transform partial differential equation with time, this make easily to find numerical solution. The solution of numerical equation is obtained from inverse transform Fourier with periodic boundary.

## 2. METHODOLOGY

### 2.1 Vorticity Equation

We consider the problem of two-dimensional turbulence where the flow is governed by Navier Stokes equation which consists of conservation of mass and momentum.

Conservation of mass

$$\nabla \cdot \mathbf{u} = 0 \quad (1)$$

momentum

$$\frac{\partial \mathbf{u}}{\partial t} + \mathbf{u} \cdot \nabla \mathbf{u} = -\frac{1}{\rho} \nabla P + \nu \nabla^2 \mathbf{u} - \frac{\mathbf{u}}{\tau} + \mathbf{F} \quad (2)$$

Where  $\mathbf{u} = [u, v]$  is a velocity vector of fluid particle,  $\rho$  is the fluid mass density,  $P$  is the pressure,  $\nu$  is the kinematic viscosity,  $\tau$  is the constant for linear friction damping and  $\mathbf{F}$  is the forcing term which can be a function of space and time [2]. The equation has 3 unknown variables, the two of velocity and the pressure  $P$ .

The vorticity equation is obtained by taking curl from Navier Stokes equation, so

$$\frac{\partial \omega}{\partial t} + \mathbf{u} \cdot \nabla \omega = \nu \nabla^2 \omega - \frac{\omega}{\tau} + f \quad (3)$$

Where  $\omega = \nabla \times \mathbf{u}$  is vorticity in the  $z$  direction and  $\mathbf{f} = \nabla \times \mathbf{F}$ . Given that  $\nabla \cdot \mathbf{u} = 0$ , then there is a scalar function  $\Psi(x, y) : \mathbf{R}^2 \rightarrow \mathbf{R}$  so that relation between velocity vector and stream function is obtained:

$$\mathbf{u} = \nabla \times \omega \quad \text{or} \quad \mathbf{u} = [u, v] = [\Psi_y - \Psi_x] \quad (4)$$

By substitution (2.4) to  $\omega = \nabla \times \mathbf{u}$ , we obtained relation between vorticity with streamfunction

$$\omega = -\nabla^2 \Psi \quad (5)$$

To reduce free parameter vorticity equation (3) we make dimensionless parameter with length scale  $L_0 = L/2\pi$ , velocity scale and time scale  $t_0 = L_0/U_0$  and

dimensionless variable  $\tilde{x} = x/L_0$ ,  $\tilde{\mathbf{u}} = \mathbf{u}/L_0$ ,  $\tilde{\omega} = \omega t_0$ .

Defining dimensionless variables to vorticity equation, we obtain normal term vorticity equation are defined on domain  $0 < x < 2\pi$  and  $0 < y < 2\pi$ .

Reynold number  $Re = L_0 U_0 / \nu$  as famous parameter dimensionless number in fluid dynamic whose represent the ratio of inertia to viscosity and the large value is indicated of turbulent flow. Next, we obtain forcing term

$$\mathbf{f} = F_0 \sin(ny) \quad \text{with } n \text{ is integer, } \beta = L_0^2 / \tau \nu.$$

Dimensionless vorticity equation without tilda term is obtained

$$\begin{aligned} \frac{\partial \omega}{\partial t} + \mathbf{u} \cdot \frac{\partial \omega}{\partial x} + \nu \frac{\partial \omega}{\partial y} \\ = \frac{1}{Re} \left( \nabla^2 \omega - \beta \omega + n(n^2 + \beta) \sin(ny) \right) \end{aligned} \quad (6)$$

The equation (6) has 2 dimensionless parameters, they are  $\beta$  and Reynolds number. This is consistent with the main objective of reducing unknown variables.

### 2.2 Equilibrium Solution

Equilibrium solution with forcing term  $\mathbf{f} = F_0 \sin(ny)$  is obtained

$$\begin{aligned} \omega &= n \sin(ny) \\ u &= \cos(ny) \\ v &= 0 \end{aligned} \quad (7)$$

$$\psi = \frac{1}{n} \sin(ny)$$

### 2.3 Spectral Methods of Vorticity Equation

In the domain  $0 \leq x \leq 2\pi$  and  $0 \leq y \leq 2\pi$ , every variable is defined as  $N \times N$  matrices. Numerically, the application of Fourier Series in vorticity equation is obtained

$$\omega(x, y, t) = \sum_{k=-\frac{N}{2}}^{\frac{N}{2}} \sum_{l=-\frac{N}{2}}^{\frac{N}{2}} \hat{\omega}_{k,l}(t) e^{ikx} e^{ily} \quad (8)$$

Where  $k, l$  are integer and  $\hat{\omega}_{k,l}$  are Fourier equation, and assumed that  $N$  is even. The coefficients Fourier can be found numerically with the used of the Fast Fourier Transform (FFT) dan the invers are Invers Fast Fourier Transform (IFFT). In Matlab we can use syntax `fft2` for FFT 2D and `ifft2` for IFFT 2D.

If vorticity is known than using the relation of vorticity and stream function, we obtained stream function 2D:

$$\psi_{k,l} = \frac{\hat{\omega}_{k,l}}{k^2 + l^2} \quad (9)$$

When  $k = l = 0$ , we defined that  $\psi_{0,0} = 0$ . By the

same way, we find relation vorticity coefficient and velocity vector

$$\begin{aligned} \hat{u}_{k,l} &= il\hat{\psi}_{k,l} \\ \hat{v}_{k,l} &= -ik\hat{\psi}_{k,l} \end{aligned} \quad (10)$$

### 3. RESULTS AND DISCUSSION

#### 3.1 Linear Part

Linear part of the vorticity equation (8) is defined:

$$\frac{\partial \omega}{\partial t} = \frac{1}{Re} (\nabla^2 - \beta) \omega \quad (11)$$

The application Fourier Transform for (11) is obtained:

$$\frac{d\hat{\omega}_{k,l}}{dt} = -\frac{1}{Re} (k^2 + l^2 + \beta) \hat{\omega}_{k,l} \quad (12)$$

Using numerically Crank Nicholson method in (12) is defined:

$$\hat{\omega}_{k,l}^{n+1} = \frac{1 - \frac{\Delta t}{2Re} (k^2 + l^2 + \beta)}{1 + \frac{\Delta t}{2Re} (k^2 + l^2 + \beta)} \hat{\omega}_{k,l}^n \quad (13)$$

For our purposes, the Crank-Nicholson method will work well [1].

#### 3.2 The Simulation Without Forcing Term

This simulation will show how the initial conditions  $\omega(x, y, 0)$  of evolve with time regardless of the forcing term. Set Reynold number  $Re = 10$ ,  $\beta = 1$ , and initial condition  $\omega = \sin(y) \cdot \sin(x)$ .

Figure 1 shows that there is a damping effect. This is as expected that the solved linear part is diffusion equation. The diffusion equation has a numerical error, damping.

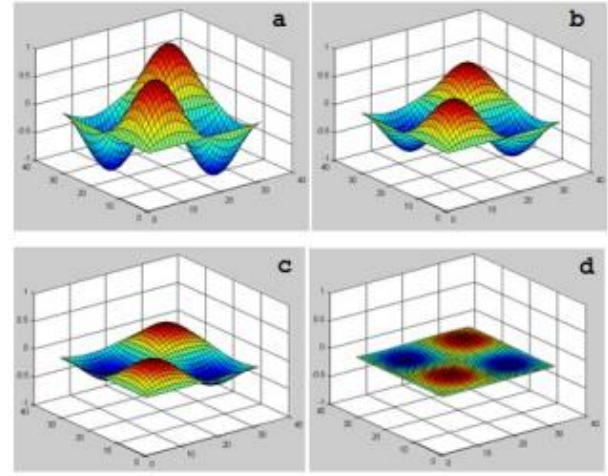


Figure 1 Simulation linear part without forcing term time by time.

#### 3.2 Linear and Nonlinear Part

The solving vorticity equation consist of linear and nonlinear parts with the application of transform Fourier:

$$\frac{d\hat{\omega}_{k,l}}{dt} = -(\mathbf{u} \cdot \nabla \omega)_{k,l} - \frac{1}{Re} ((k^2 + l^2 + \beta) \hat{\omega}_{k,l}) + \hat{f}_{k,l} \quad (14)$$

as  $\hat{f}$  is Fourier transform of  $f = 1/Re \cdot n(\beta + n^2) \sin(ny)$ .

By using Crank Nicholson method, we solved the vorticity equation (14)

$$\hat{\omega}_{k,l}^{n+1} = \frac{\frac{\Delta t}{2} \left( 3(\mathbf{u} \cdot \nabla \omega)_{k,l}^n - ((\mathbf{u} \cdot \nabla \omega)_{k,l}^n + \left(1 - \frac{\Delta t}{2Re} (k^2 + l^2 + \beta)\right) \hat{\omega}_{k,l}^n + \Delta t \cdot \hat{f}_{k,l} \right)}{1 + \frac{\Delta t}{2Re} (k^2 + l^2 + \beta)} \quad (15)$$

The (15) equation will be used in Matlab [1].

#### 3.3 Simulation with Forcing Term

$$1/Re \cdot n(\beta + n^2) \sin(ny)$$

Set forcing term  $f = 1/Re \cdot n(\beta + n^2) \sin(ny)$ , initial condition  $\omega = n \sin(ny)$ ,  $Re = 60$  and  $\beta = 32$ .

From Figure 2, the solution of vorticity shows that no changes time by time. This happen because the initial condition is equilibrium solution.

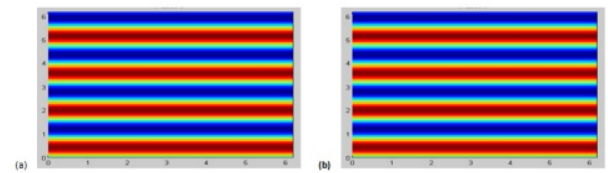


Figure 2 Simulation vorticity without forcing term.

#### 3.3 Simulation with Enlarged Forcing Term

Now, we show how stability solution work if forcing term enlarge, with Matlab use

$$f = 1/Re * n * (\beta + n^2) \sin(ny) + 0.1 * randm(size(y)).$$

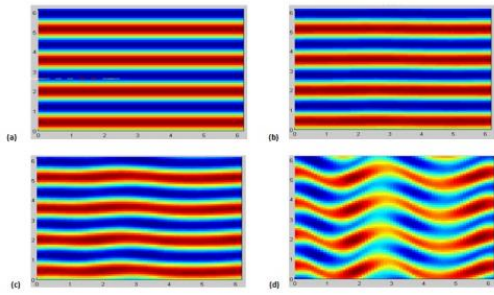


Figure 3 Simulation results with enlarged forcing term.

The above solution shows us that an enlarged forcing term will cause an unstable low. In a long time, it will cause turbulent flow. The turbulent nature of fluid flow depends on the size of Reynolds number parameter. The larger Reynolds number make the flow became faster turbulent.

#### 4. CONCLUSION

The application of the spectral method with Fourier series expansion can be carried out on 2D fluid flow. The application of this spectral method can be producing simulation that show a steady of fluid and can also show turbulence of fluid flow.

#### REFERENCES

- [1] Storey, B. D. (2012). Modelling 2D Turbulence. *Modelling Franklin W.Olin College of Engineering*, 1-10.
- [2] Zhou, Y., Luo, Z., & Teng, F. (2018). A Crank–Nicolson finite spectral element method for the 2D non-stationary Stokes equations about vorticity–stream functions. *Journal of Inequalities and Applications*, 2018(1), 320.

# DeltaEC prediction of pressure along a quarterwave thermoacoustic test rig

Dahlia Johari<sup>1</sup>, Ernie Mattokit<sup>1,2,\*</sup>, Fatimah Al Zahrah Mohd Saat<sup>1,2</sup>, Normah Mohd Ghazali<sup>3</sup>

<sup>1</sup>) Fakulti Kejuruteraan Mekanikal, Universiti Teknikal Malaysia Melaka, Hang Tuah Jaya, 76100 Durian Tunggal, Melaka, Malaysia

<sup>2</sup>) Centre for Advanced Research on Energy, Universiti Teknikal Malaysia Melaka, Hang Tuah Jaya, 76100 Durian Tunggal, Melaka, Malaysia

<sup>3</sup>) Faculty of Engineering, Universiti Teknologi Malaysia, 81310 Skudai, Johor, Malaysia

\*Corresponding e-mail: ernie@utem.edu.my

**Keywords:** Thermoacoustics; DELTAEC; standing wave

**ABSTRACT** – This paper reports thermoacoustic models for a standing wave type resonator with quarter wavelength design and frequencies of 14.2 Hz and 23.6 Hz. The models were solved using a thermoacoustic design software known as DELTAEC. The result of pressures distribution across the resonator was discussed based on the converged models. It was observed that by using 200 mm-long stack, pressure drops as much as 806.6 Pa and 834.3 Pa at stack's location of  $0.19\lambda$  and  $0.11\lambda$  for 14.2 Hz and 1.0 drive ratio. At the same frequency and drive ratio, longer stack causes higher pressure drop of 806.6 Pa as compared to shorter stack with 777.5 drops in pressure. Using 200 mm-long stack, pressure drops as much as 1204.9 Pa (23.6 Hz, drive ratio of 1.35) as compared to 806.6 Pa (14.2 Hz, drive ratio of 1.0).

## 1. INTRODUCTION

Thermoacoustics is a principle of science that can be used to produce a generator or a cooler if specific conditions are met [1,2]. At this moment, the fluid dynamics of flow inside the system is not well known, therefore investigation is needed in this direction [3]. However, investigating the fluid dynamics phenomena requires development of experimental rig that can produce the thermoacoustic field. Therefore, the system needs to be designed carefully at early stage of investigation to avoid too much expensive expenditure. In thermoacoustic community, this is usually done through a design software known as DeltaEC [4]. The design software helps designer to assemble parts into the model and then solve the model so that flow distribution inside the system is in accordance to the thermoacoustic principle. Although, the system has been designed by many in another parts of the world [1,2,5], but investigation here in Malaysia is very scarce. This paper reports an initial effort of modelling thermoacoustic resonator using DELTAEC for the purpose of the investigation of fluid dynamics of flow inside a standing

wave rig with quarter wavelength resonator.

## 2. METHODOLOGY

The standing wave thermoacoustic model was designed using a software known as DELTAEC. Figure 1 shows the segments that were defined in DELTAEC. It consists of a 'Begin' segment that allows the setting up of the initial values and operating conditions for the numerical modelling. The 'begin' segment is then connected to a 'duct' labelled 1 which represented loudspeaker.

The loudspeaker was connected to segment 2 named as a 'short duct'. This segment was to be considered the box for the loudspeaker to enclose the sound that came out of the loudspeaker and this sound was then channeled into the resonator through segment 3 (a conical duct). Segment 4 which was known as 'minor' is introduced into the model to represent losses of the flow when it was being forced into the resonator through the converging channel. The resonator started at segment 5 and ended at segment 15. The total length of the resonator was 6.6 m. The stack was located in segment 7 and it was sandwiched between segments 6 and 8. The presence of big number of segments in the resonator was due to the design requirement so that the rig could be used for two different flow frequencies. The schematic diagram shown in Figure 1 represents the 14.2 Hz resonator. Investigation was also done for another frequency of 23.6 Hz. The DELTAEC model for 23.6 Hz is as shown in Figure 2.

For high frequency of 23.6 Hz, the total length of the resonator was 3.8 m. Therefore, the total number of segments were now reduced to 10. In this 23.6 Hz model, the stack was located in segment 6 of Figure 2.

The models were solved for several cases as summarized in Table 1. The stack was located at two locations of  $0.19\lambda$  and  $0.11\lambda$  relative to the hard end of the resonator (pressure antinode location).

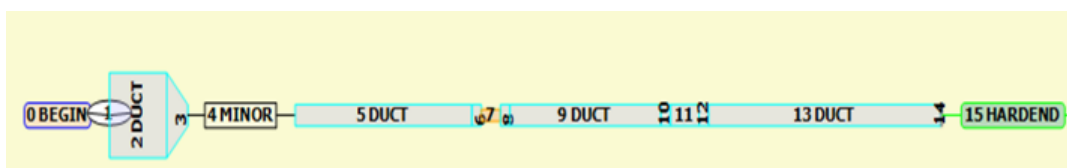


Figure 1 The 14.2 Hz thermoacoustic model.

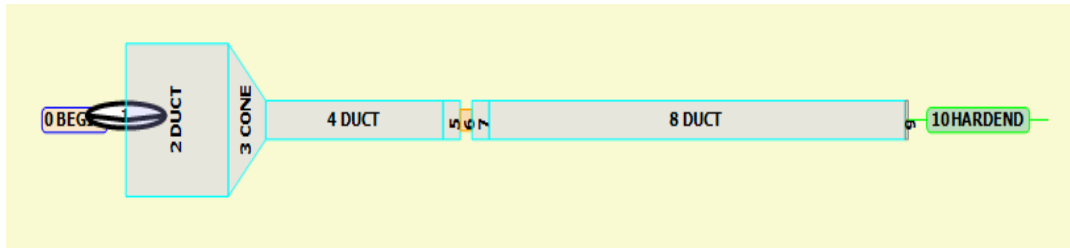


Figure 2 The 23.6 Hz thermoacoustic model.

Table 1 Summary of cases for thermoacoustics models.

Case	Frequency (Hz)	Stack's length (mm)	Stack's location
1	14.2	200	$0.19\lambda$
2	14.2	200	$0.11\lambda$
3	14.2	70	$0.19\lambda$
4	23.6	200	$0.19\lambda$
5	23.6	70	$0.19\lambda$

### 3. RESULTS

Figure 3 shows the pressure distribution plotted data for cases 1, 2 and 3, which is explained accordingly to Equation 1 and calculated from the pressure antinode at the right end of the resonator (segment 15).

$$p_1 = p_a e^{i\omega t} \cos(kx) \quad (1)$$

An empty resonator (without stack) leads to decrement in pressure with locations according to standing wave characteristics. The presence of 200 mm stack in the resonator leads to pressure drops depending on the location of the stack. When the stack is located at  $0.19\lambda$ , the pressure drop is appeared at segment 6. For location of  $0.11\lambda$ , the pressure starts dropping in segment 10. It is also observed that the pressure drops steeper than the pressure drop without stack. Pressure drops within the stack at  $0.19\lambda$  is found to be higher as much as 806.6 Pa than when the stack is placed at  $0.11\lambda$  with 834.3 Pa drops.

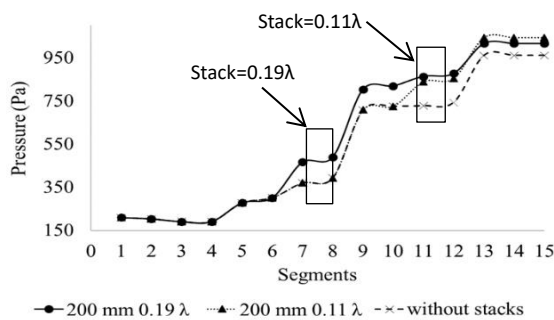


Figure 3 Pressure distribution for cases 1, 2 and 3 (14.2 Hz, drive ratio of 1.0).

Figure 4 depicted the effect of stack's length located at  $0.19\lambda$ , on the pressure distribution. As expected, the pressure drop is smaller with 777.5 Pa for case with shorter stack. The presence of the 70 mm long stack has very little impact on pressure distribution inside the resonator and seemed to be unnoticeable as compared to 200 mm length stack. Higher pressure drop of 806.6 Pa is attained throughout longer stack which might due to longer obstruction faced by the air flow. The boundary layer development might also be the reason that reducing

the air velocity, and yet dropping the pressure flow.

Figure 5 shows the pressure distribution data for two different flow frequencies and drive ratio. Pressure drop is not the function of the wavelength, but the wavelength is a function of frequency. For 23.6 Hz-designed system, pressure drops as much as 1204.9 Pa for 200 mm long stack, and 1112.5 Pa for 70 mm long stack respectively. However, for 14.2 Hz-designed system, less pressure drops are predicted as much as 806.6 Pa for 200 mm long stack, and 777.5 Pa for 70 mm long stack respectively. The predicted data from DELTAE is then used for designing thermoacoustic system for further study in this work.

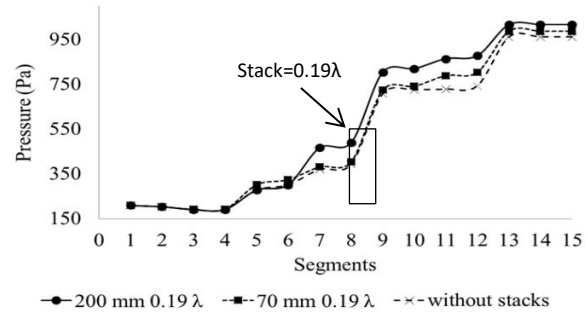


Figure 4 Pressure distribution for cases 1 and 3 (14.2 Hz, drive ratio of 1.0).

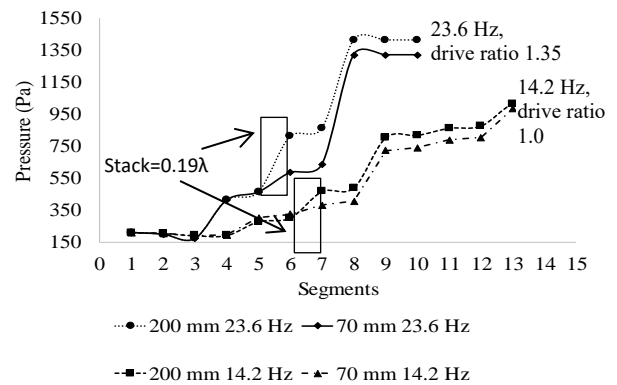


Figure 5 Pressure distribution for cases with different stack's length, frequency and drive ratio.

### 4. SUMMARY

The predicted work can be summarized as listed here:

- By using 200 mm-long stacks, pressure drops as much as 806.6 Pa and 834.3 Pa at stack's location of  $0.19\lambda$  and  $0.11\lambda$  for 14.2 Hz and 1.0 drive ratio.
- At the same frequency and drive ratio, longer stack causes higher pressure to drop of 806.6 Pa as compared to shorter stack with 777.5 drops in

pressure.

- (c) By using 200 mm-long stacks, pressure drops as much as 1204.9 Pa (23.6 Hz, drive ratio of 1.35) as compared to 806.6 Pa (14.2 Hz, drive ratio of 1.0).

## REFERENCES

- [1] Abdoulla-Latiwish, K. O., Mao, X., & Jaworski, A. J. (2017). Thermoacoustic micro-electricity generator for rural dwellings in developing countries driven by waste heat from cooking activities. *Energy*, *134*, 1107-1120.
- [2] Sharify, E. M., & Hasegawa, S. (2017). Traveling-wave thermoacoustic refrigerator driven by a multistage traveling-wave thermoacoustic engine. *Applied Thermal Engineering*, *113*, 791-795.
- [3] Mohd Saat, F., & Jaworski, A. (2017). Numerical predictions of early stage turbulence in oscillatory flow across parallel-plate heat exchangers of a thermoacoustic system. *Applied Sciences*, *7*(7), 673.
- [4] Swift, G. W. (2017). *Thermoacoustics: A unifying perspective for some engines and refrigerators*. Springer.
- [5] Saechan, P., & Jaworski, A. J. (2019). Numerical studies of co-axial travelling-wave thermoacoustic cooler powered by standing-wave thermoacoustic engine. *Renewable Energy*, *139*, 600-610.



# Continuous water quality monitoring for water hydraulics applications in food processor

Ahmad Anas Yusof<sup>1,2,\*</sup>, Suhaimi Misha<sup>1,2</sup>, Syarizal Bakri<sup>1,2</sup>

<sup>1)</sup>Fakulti Kejuruteraan Mekanikal, Universiti Teknikal Malaysia Melaka, Hang Tuah Jaya, 76100 Durian Tunggal, Melaka, Malaysia

<sup>2)</sup>Centre for Advanced Research on Energy, Universiti Teknikal Malaysia Melaka, Hang Tuah Jaya, 76100 Durian Tunggal, Melaka, Malaysia

\*Corresponding e-mail: anas@utem.edu.my

**Keywords:** Water hydraulics; water quality; sustainability

**ABSTRACT** – This study proposes an application of water hydraulics technology in a food processor for a traditional cookies production. The objective of the study is to provide a hygienic and safe condition for water hydraulics that is used in a food processor test bed. The test bed is tested by using distilled water, and operated for duration of six months. The quality of the water used in the system is monitored and tested for total dissolved solids and pH value. The result shows that the pH value can be stabilized by using a filtration system, while total dissolved solids continues to accumulate throughout the test duration.

## 1. INTRODUCTION

Water hydraulics encourages a sustainable approach in power transmission. [1-3]. The objective of this project is to monitor the quality of a water-based pressure medium that is used to power up a food processor system. The hygienic, safe and low maintenance cost characteristics of water should provide interesting viewpoints due to concern over issues in hydraulic fluid contamination, flammability, disposal, and costly maintenance. Thus, the project focuses on the development of a traditional food processor apparatus powered by water hydraulics. The quality of the water used in the power transmission medium is tested for pH and TDS readings [4-7]. A test rig consists of two water hydraulics cylinders have been developed for the system and assembled into a robotic manipulator driven by a low-cost water hydraulic system. The cylinders have double acting configuration, with bore size and stroke of 40 mm and 125 mm respectively. The system resembles an automated cookies extrusion system, whereby the cookie dough is pressed to form a unique shape for the cookies [8].

## 2. METHODOLOGY

The test rig (Figure 1) has been setup to work in an automatic mode in producing batches of cookies continuously. The water qualities data obtained are on weekly period for nine months, from June 2017 to March 2018. A stainless steel in-line water filter has been assembled during the second run of the test, between January to March 2018. The samples are taken from the water tank after every usage. They are tested three times per week and taken before and after the experiment. A TDS-3 digital PH and TDS meter are used in the measurement of the water quality.

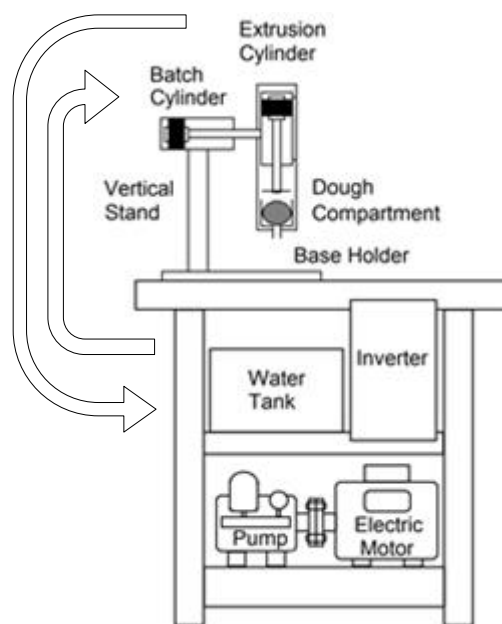


Figure 1 Water quality monitoring of water hydraulics flow.

## 3. RESULTS AND DISCUSSION

Figure 2 shows the result obtained for pH measurement. A control sample in the form of distilled water is used as a reference, where the pH reading of 7.66 is recorded. It is recorded that in between September and November 2017, the test rig shows an increase in pH values. This is noted when the experiment is conducted without the installation of a high-pressure water filter. The filter was later installed in November 2017. In between November and December 2017, the pH value is noted to be increased. It is possible that the pH measurement is high due to the prolong unused operation for the food processor. In general, however, the overall pH readings are acceptable to reduce corrosion effect. It is noted that corrosion will aggressively occur below pH 4. In between pH 4 to pH 10, corrosion is independent of pH value. [9-10]. In 2018, the test continues from January till March. It is noted that within that period, the pH values of the water is at a constant pH 7.8. The values coincide with the installation of the water filter and the constant usage of the system starting from January 2018.

